

Role of Crystallographic Texture in Hydrogen-Induced Cracking of Low Carbon Steels for Sour Service Piping

V. VENEGAS, F. CALEYO, J.M. HALLEN, T. BAUDIN, and R. PENELLE

This work presents the results of ongoing investigations aimed at determining the influence of crystallographic texture on hydrogen-induced cracking (HIC) in low carbon steels for sour service piping. Electron backscatter diffraction (EBSD) and X-ray texture measurements have been performed on HIC samples of API 5L X46 and ASTM A106 steels. The results obtained in this study show that the resistance to HIC of low carbon steels for sour service piping could be improved through crystallographic texture control and grain boundary engineering. Controlled rolling schedules can be proposed in order to induce a crystallographic texture dominated by the $\{112\}/\text{ND}$, $\{111\}/\text{ND}$, and $\{011\}/\text{ND}$ fibers, where ND is the sample normal direction. Such a texture is expected to decrease significantly the steel susceptibility to HIC by (1) reducing the number of available transgranular and intergranular low resistance cleavage paths provided by the $\{001\}/\text{ND}$ oriented grains, (2) reducing the probability of crack coalescence and stepwise HIC propagation through large HIC-induced plastic strain, and (3) increasing the number of high resistance intergranular crack paths provided by coincidence site lattice (CSL) boundaries and low-angle boundaries between grains with orientation within the $\{111\}/\text{ND}$ texture fiber.

DOI: 10.1007/s11661-007-9130-9

© The Minerals, Metals & Materials Society and ASM International 2007

I. INTRODUCTION

HYDROGEN-INDUCED cracking (HIC) occurs in low carbon steels used in line pipes and pressure vessels carrying wet sour hydrocarbons. The nascent hydrogen produced at the corroding pipe surface diffuses into the steel and precipitates as molecular hydrogen at nonmetallic inclusions, ferrite-pearlite interfaces, martensite islands, and grain boundaries.^[1] At these traps, the pressure developed by molecular hydrogen increases to a level at which cracks initiate and propagate either in a straight way parallel to the rolling plane or in a stepwise manner.^[1-4]

The resistance to HIC of sour service steels can be improved by adopting several strategies. Among them, the reduction in sulfur content, the control of inclusion morphology, and the use of low segregated, uniform microstructures are the most adopted.^[1,5] These strategies have proven not to be totally effective in the prevention of HIC in severe conditions.^[1,4,6] Therefore, the control of other metallurgical aspects that could improve HIC resistance is desirable. In this sense, the control of crystallo-

graphic texture (or simply texture or macrotexture*)

*The terms macrotexture, microtexture, and mesotexture refer to the average sample texture, the crystallographic orientation of a microstructure point, and the texture of grain boundaries, respectively.^[7]

and grain boundary distribution (or mesotexture)^[7] seems to be a logical step toward this goal.

The fact that texture can play a significant role on fatigue crack growth has been corroborated through experimental and modeling studies.^[8,9] Texture is also expected to play a major role in reducing HIC, because it can determine the availability of low resistance paths for crack propagation. In addition to that, texture can be effectively controlled during the steel forming process.^[10] In one of the earliest attempts to consider texture with regard to HIC, Miyoshi *et al.*^[3] showed that carbon-manganese steel specimens with a marked $\{001\}$ - $\{113\}/\text{ND}$ ** texture

**The notation $\{hkl\}/\text{ND}$ indicates that the $\{hkl\}$ planes lie parallel to the rolling plane.^[7]

manifest a larger resistance to HIC than specimens with nearly random texture. Surprisingly, these authors concluded that the influence of texture to HIC was not significant. In contrast, Verdeja *et al.*^[4] have recently postulated that the presence of a $\{110\}$ - $\{332\}/\text{ND}$ texture is expected to reduce the sensitivity to HIC of ferritic-pearlitic steels, while the presence of a $\{001\}$ - $\{113\}$ - $\{112\}/\text{ND}$ texture will produce the opposite effect.

V. VENEGAS, Postdoctoral Fellow, F. CALEYO, Associate Professor, and J.M. HALLEN, Professor, are with the Departamento de Ingeniería Metalúrgica, IPN-ESIQIE, UPALM Edif. 7, Zacatenco, México, D.F. 07738, México. T. BAUDIN, Professor, and R. PENELLE, Professor, are with the Laboratoire de Physico-Chimie de l'Etat Solide, ICMMO, UMR CNRS 8182, Bâtiment 410, Université de Paris Sud, 91405, Orsay, Cedex, France. Contact e-mail: fcaleyo@gmail.com

Manuscript submitted October 9, 2006.

Article published online April 21, 2007.

At the atomic scale, the mechanisms observed for HIC are those of hydrogen-enhanced decohesion (HEDE), absorption-induced dislocation emission (AIDE), and hydrogen-enhanced plasticity (HELP).^[11] The AIDE has been observed to be mainly associated with cleavagelike fracture and dimpled intergranular fracture. In contrast, HELP has been related to slip-band fractures, while HEDE seems to dominate in brittle intergranular fractures. The common factor to all these mechanisms is that crack propagation depends strongly on the crystallographic orientation of the material relative to the crack tip. Therefore, when investigating the role of crystallographic orientation on HIC, it is of paramount importance to consider the microtexture and mesotexture of the material rather than to consider only its macrotexture.

This work presents the results of ongoing investigations aimed at determining the influence of macrotexture, microtexture, and mesotexture on HIC in low carbon steels for sour service piping. HIC samples of API-5L-X46 and ASTM-A106 steels have been investigated using X-ray diffraction and EBSD together with orientation imaging microscopy (OIM).^[7,12] From these measurements, the influence of crystallographic orientation on hydrogen-induced crack propagation, interaction, and coalescence has been investigated, focusing on three main aspects: the influence of grain orientation on transgranular crack propagation along cleavage and slip planes, the influence of grain orientation on the plastic strain induced by the interaction of closely spaced non-coplanar cracks, and the role of grain boundary distribution in providing weak paths for intergranular crack propagation.

II. EXPERIMENTAL MATERIALS AND PROCEDURES

The HIC was investigated in two steels for which the composition is shown in Table I. Samples of steel A were taken from an HIC-damaged section of a 610-mm diameter, 12-mm thickness, API-5L-X46 pipeline, which transported wet sour gas for about 25 years. Plates of steel B were taken from a new 610-mm diameter, 12-mm thickness, ASME-A106 grade B line pipe. For this steel, HIC tests were conducted following the NACE TM0284-96 standard (with the TM 0177 solution) to produce HIC samples from these plates. This standard provides a test method for assessing the resistance of pressure vessel steels to HIC produced by hydrogen absorption from aqueous sulfide corrosion.^[13]

The X-ray texture of the investigated steels was measured on the rolling plane (defined by the rolling RD and transverse TD directions) of one-quarter and

half-thickness samples. Three incomplete pole figures, {110}, {200}, and {111}, were measured using a Mo goniometer. The orientation distribution function (ODF) of each sample was determined from the measured pole figures using the ADC method.^[14] The Bunge's Euler angles were adopted to describe orientations, and the $\varphi_2 = 45$ deg section of Euler space was used to display the computed ODFs.^[7]

Scanning electron microscopy and automated field emission gun-EBSD were used, respectively, to perform metallography inspections and to collect microtexture data on transversal sample cross sections (defined by the transverse TD and normal ND directions) of the investigated HIC samples. The OIM was used to analyze the EBSD measurements performed on a hexagonal grid with a spacing ranging from 0.1 to 3 μm . The distributions of individual grain orientations, of EBSD pattern quality (IQ) and of grain orientation spread[†] values,

[†]Defined as the average of the misorientation angles between all points in the grain.^[12]

were mapped for each measured HIC region. Grain boundaries were defined in the EBSD-derived microstructures by the presence of point-to-point misorientations greater than 3 deg. The grain boundary classification adopted was as follows: (1) low-angle boundaries (LABs) with misorientation angle less than 15 deg, (2) high-angle (general-disordered) boundaries (HABs), and (3) coincidence site lattice (CSL, Σn) boundaries satisfying the Brandon criterion,^[7] $\Sigma 29$ being the highest CSL considered.

The numerical simulation of the stress state ahead of crack tips and in the region between closely spaced, non-coplanar cracks was performed assuming an isotropic linear elastic material in plane stress condition. The stress intensity factors for the mixed mode of loading in this region and the resulting maximum shear and largest principal stresses were computed using methods described elsewhere.^[15,16,17]

III. RESULTS AND DISCUSSION

A. Metallographic Inspection

Figure 1 shows typical SEM micrographs taken from the TD-ND section of HIC samples of steels A and B after mechanical and electropolishing, followed by etching with 2 pct Nital and Superpicral, respectively.

Steel A has a pearlite/ferrite microstructure with a ferrite grain size of about 20 μm and a proportion of pearlite close to 30 pct. The main sites for HIC nucleation in these steels were elongated (type II) MnS inclusions. Steel B shows a more banded pearlite/ferrite microstructure with a reduced pearlite proportion (~8 pct) and a ferrite grain size close to 15 μm . In this material, the MnS inclusions were found to be much less numerous with spherical shape. Consequently, HIC nucleation sites were found located primarily at ferrite/pearlite interfaces. Despite the fact that steel B has a

Table I. Chemical Composition of the Investigated Steels (Weight Percent)

Steel	C	Mn	S	P	Si	Cu	Cr
A	0.212	1.334	0.032	0.028	0.037	—	0.009
B	0.085	0.916	0.009	0.017	0.252	0.272	0.011

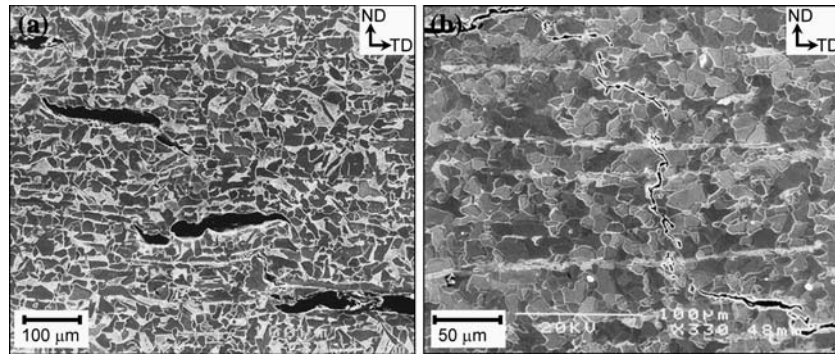


Fig. 1—Typical transversal (TD-ND) microstructures of HIC samples of steels (a) A and (b) B.

reduced sulfur and manganese content, it shows all the features typical of HIC damage.

In steel A, the HIC damage is far more severe, with cracks greater in number and larger in size than the cracks in steel B. It is common to these two steels that the hydrogen-induced cracks grow parallel to the rolling plane following intergranular and transgranular paths, the former being the predominant crack propagation mode. In most of the observed cases, the tips of close spaced cracks deflect toward each other along the normal direction. This deflection, which results from crack interaction, leads in some cases to the coalescence of the interacting cracks and thereby to stepwise HIC propagation. In other cases, this interaction does not result in crack merging and the interacting crack tips run around each other without further growth. The microscopic details of crack

growth and crack interaction are investigated in Section III-D.

B. Macrotexture

Figure 2 shows the experimental $\{200\}$ pole figures and the computed $\varphi_2 = 45$ deg ODF sections for the center samples of the investigated steels. These textures were very much like those observed in the quarter-thickness samples so that through-thickness texture variations were not addressed in this study.

A nearly random texture was observed in steel A. This texture is typical of low carbon steels finished using an austenitic hot rolling strategy.^[10] However, the ODF of this steel reveals the presence of a weak departure from randomness at orientations within 15 deg of the ideal rotated cube $\{001\}\langle 110 \rangle$ and $\{112\}\langle 110 \rangle$

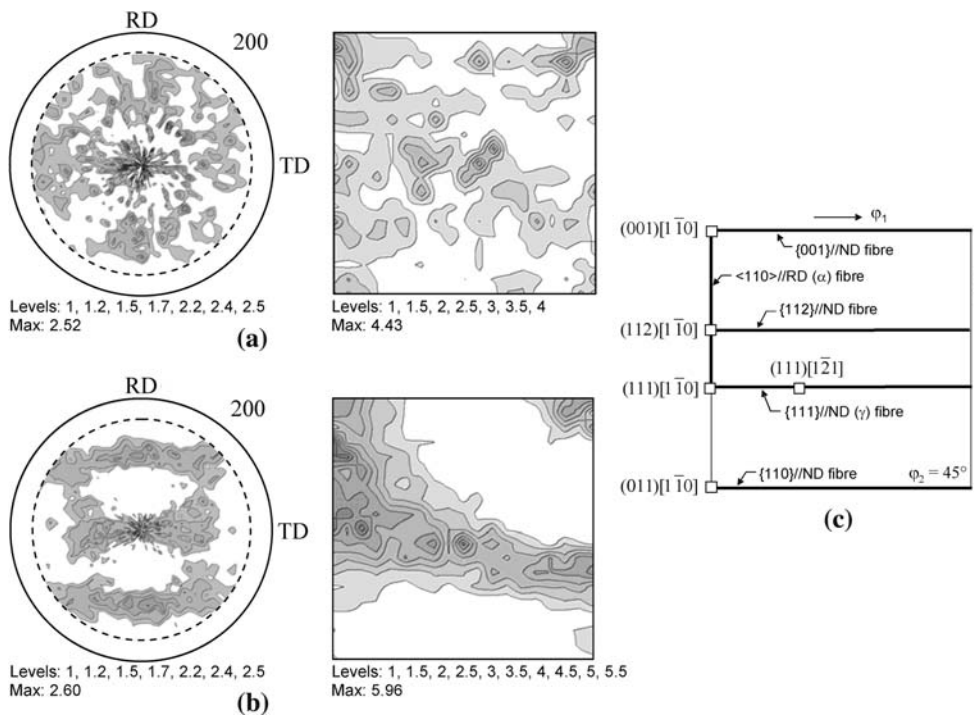


Fig. 2—Experimental $\{200\}$ pole figures and $\varphi_2 = 45$ deg sections of the ODFs of steels (a) A and (b) B. (c) Texture component key to the $\varphi_2 = 45$ deg section.

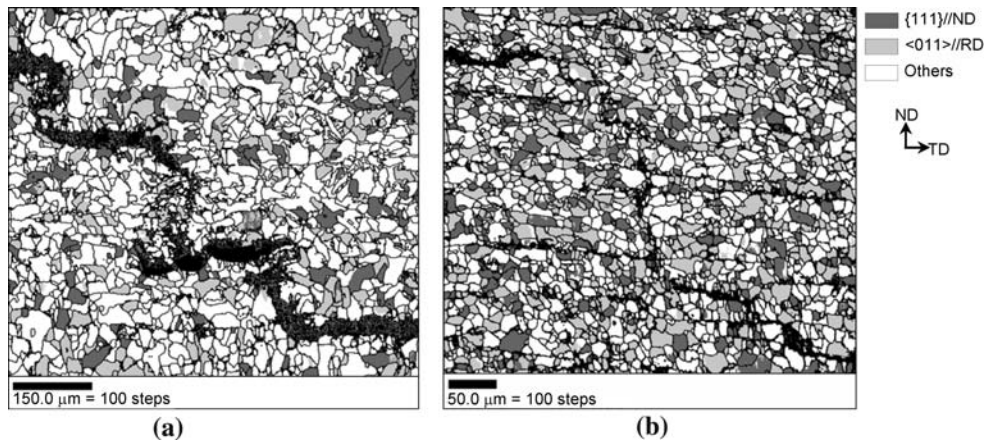


Fig. 3—OIM maps derived from the EBSD measurements taken at the TD-ND sections shown in Fig. 1 for steels (a) A and (b) B. Grains with orientation within 15 deg of the ND and RD fibers are shaded as marked in the figure legend.

orientations. The most noticeable feature of the texture of this material is the weakness of the $\{111\}$ //ND fiber, also known as ND or γ fiber.

On the other hand, steel B displays a strong texture characteristic of recrystallized ferrite (warm) rolled bcc materials.^[10] This consists of a dominant RD (α) fiber ($\langle 110 \rangle$ //RD) together with a complete $\{111\}$ /ND fiber. In this steel, the ODF maximum is observed at the $\{111\} \langle 110 \rangle$ component.

C. Orientation Maps

Figure 3 shows the orientation maps derived from the EBSD measurements of the HIC regions shown in Figure 1. A simple coding system is used in this figure to distinguish the grains with orientations within 15 deg of the ideal orientations belonging to the RD and ND texture fibers. The white grains have orientations outside these two fibers. Grain boundaries are drawn for grain

misorientation equal or larger than 15 deg. The black regions correspond either to cracks or to unresolved cementite in pearlite.

The microstructural and texture data extracted from the orientation maps shown in Figure 3 (and those not shown here) agreed closely with the results obtained using conventional metallography and X-ray measurements, respectively. In addition to that, the microtexture measurements did not evidence the presence of strong local texture inhomogeneities in the studied HIC regions such as orientation clustering.

D. Role of Orientation on Crack Propagation

This investigation corroborates previously published results^[3,4,18] showing that transgranular HIC propagation takes place mainly through cleavage and, in a very few cases, *via* slip-related fracture. Figure 4 shows examples of transgranular HIC propagation observed

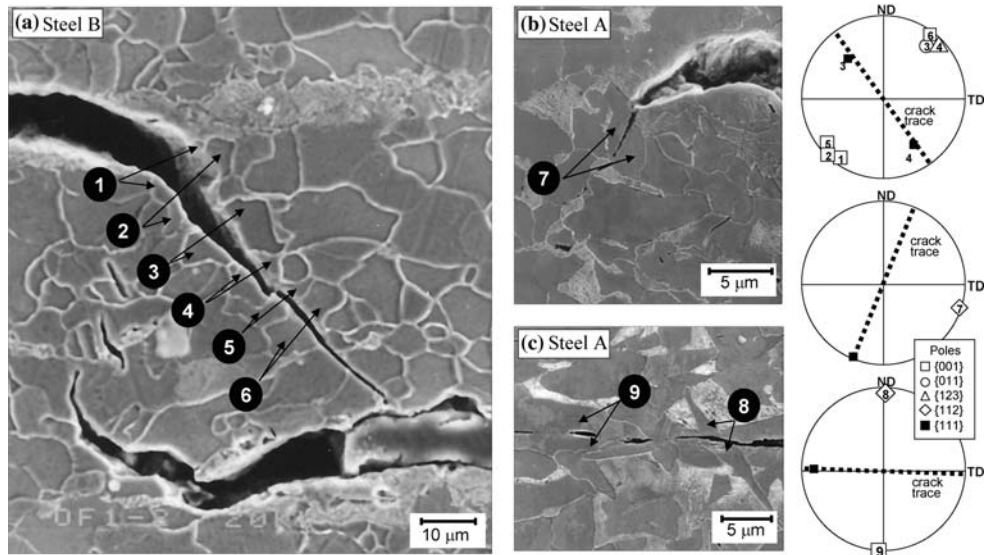


Fig. 4—Examples of intragranular HIC propagation in the investigated steels. The stereographic projections give the position of the cleavage plane and slip system closest to the crack trace in the identified fractured grains.

in the steels under investigation. To carry out this analysis, the grains fractured in a transgranular mode were first located through metallographic inspection. Then, the disorientation between the material regions separated by the crack was determined. These regions were assumed to belong to the same grain when the disorientation angle between them was less than 3 deg. After that, the orientation of the cracked grains was used to plot the poles of the cleavage planes and slip systems in the stereographic projection. The plane with the smallest angular distance to the crack trace was assumed to be that in which the crack propagated in a transgranular mode.

Cleavage along the $\{001\}$ planes was found to be the main cause of transgranular crack growth in the rolling plane as well as of crack deflection in the ND direction (grains 1, 2, 5, and 6). Transgranular propagation in the $\{011\}$, $\{112\}$, and $\{123\}$ families of slip planes was also observed mainly at deflected crack tips (grains 3, 4, 7, and 9). In a very few cases, this kind of propagation was observed contributing to crack propagation in the rolling plane (grain 8).

It is easy to show that the orientation of the crack traces in the HIC microstructures in Figure 4 can be related to the state of stress ahead of the interacting crack tips and in the region between them. The stress field in these regions is characterized by a mixed-mode (modes I and II) loading induced by the crack interaction process.^[15,16,17] As an example, Figure 5 shows a numerical simulation of the spatial distribution of the maximum shear (τ_{\max}) and largest principal (σ_{\max}) stresses in the region between the cracks shown in Figure 4(a). This distribution was obtained numerically for the crack interaction model shown in Figure 5(a) with $h/a = 0.5$ and $d/a = 0.1$. These parameters allow the stress condition before crack overlapping to be simulated. The stress intensity factors, K_I and K_{II} , and the values of τ_{\max} and σ_{\max} were computed for each location in this region using methods described elsewhere.^[15,16,17]

The combined analysis of Figures 4 and 5 corroborates the significant role that microtexture can play in affecting the crack interaction and coalescence process. In the presence of cleavage planes and slip systems suitably oriented relative to the stress field, crack

coalescence can occur in an anisotropic manner for crack configurations with a value of h/a that can be larger than that predicted (0.28) by the isotropic, mixed-mode fracture mechanics.^[15] For example, the downward deflection suffered by the upper crack in Figure 4(a) is much more significant than the upward deviation experienced by the lower crack. Due to the symmetry of the interaction, the isotropic mixed-mode fracture mechanics is unable to explain such an interaction pattern. The explanation comes from the fact that cracking occurred along cleavage planes in grains 1, 2, 5, and 6 and along slip planes in grains 3 and 4. These planes provided weak propagation paths because they are suitably oriented with respect to the largest principal stress (grains 1, 2, 5, and 6) and maximum shear stress (grains 3 and 4) depicted in Figure 5.

It is worth noting that the shear dominated fracture observed in grain 7 of Figure 4(b) can also be related to the state of stress ahead of the crack tip predicted by Figure 5(c).[‡]

[‡]After flipping Fig. 5(c) horizontally to produce a crack interaction configuration similar to that of Fig. 4(b).

Additionally, Figure 5(b) reveals the driving force for the nucleation of the newly formed small cracks observed between the interaction tips in Figure 4(a). For example, in Figure 5(b), the largest principal stress is predicted almost perpendicular to the small cracks observed in Figure 4(a). The favorable stress direction, combined with the sharp increase in the mode I (opening) stress before crack tips meet,^[15] may have triggered the nucleation of these newly formed cracks.

With regard to grain orientation, the low resistance cleavage paths associated with transgranular HIC in the rolling plane were found to be provided mostly by grains with orientations within 15 deg of the ideal $\{001\}$ //ND fiber. On the other hand, crack-tip deflection in the normal direction due to crack interaction was found to be associated with transgranular propagation along cleavage and slip planes in grains with orientations of the $\{001\}$ //ND, $\{111\}$ //ND, and $\langle 011 \rangle$ //RD fibers.

The relationship between grain orientation and crack path is further investigated in Figure 6. The $\varphi_2 = 45$

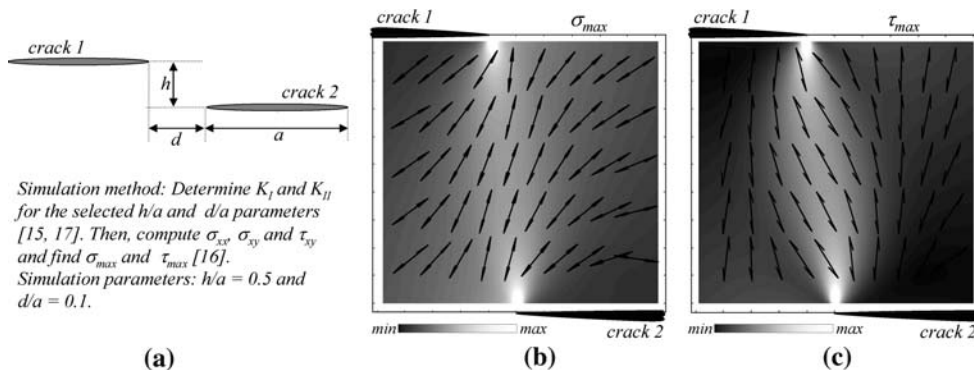


Fig. 5—Simulated stress field in the region between two close cracks before overlapping (Fig. 4 (a)). (a) Crack interaction model, (b) largest principal stress, and (c) maximum shear stress. The magnitude of the stress field is coded in gray shades. The stress direction is indicated by the arrows.

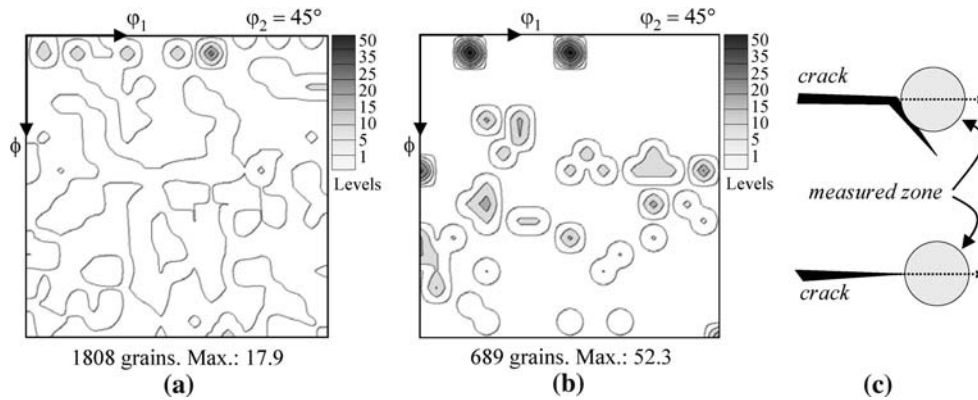


Fig. 6— $\varphi_2 = 45$ deg sections of the ODFs computed from individual grain orientations in steel A for grains (a) along crack paths (at both crack sides) and (b) immediately ahead of crack tips, along the original crack direction, as shown in (c).

deg section of the ODF, computed from the individual orientations of more than 1,800 grains along crack paths in steel A, is shown in Figure 6(a). The HIC propagation is mainly associated with grains with orientations of the $\{001\}$ //ND type. This can be related to the fact that cleavagelike propagation in the rolling plane is enhanced in materials with a large number of $\{001\}$ //ND rotated cube grains. It is also reasonable to postulate that the tilt LABs between grains with orientations of this fiber can provide weak intergranular paths on which cleavagelike propagation can occur by absorption-induced dislocation emission.^[11]

On the other hand, Figure 6(b) shows the $\varphi_2 = 45$ deg section of the ODF computed from the individual grain orientations of more than 650 grains located immediately ahead of several crack tips in steel A (Figure 6(c)). A comparative analysis of the ODFs shown in Figures 6(a) and (b) reveals that the probability that HIC cracks arrest or deflect in the pipe's normal direction increases when the crack fronts encounter grains with orientations within the $\{111\}$ //ND, $\{112\}$ //ND, and $\{011\}$ //ND fibers.

The transgranular propagation of HIC in the rolling plane produced by slip-related fracture can be predicted to be very unlikely (though not impossible, *e.g.*, grain 8 in Figure 4(c)) in a steel with a texture dominated by these three texture fibers. The $\{111\}$ //ND, $\{112\}$ //ND, and $\{011\}$ //ND orientations will increase the proportion of high resistance paths for straight HIC propagation because they lead to a reduction in the number of cleavage planes suitably oriented relative to the rolling plane. It is also important to consider that, for mode I loading, the shear stress is null ahead of the crack tips. Therefore, a shear-related fracture in the $\{111\}$ //ND, $\{112\}$ //ND, and $\{011\}$ //ND oriented grains will always move the crack trace off the rolling plane (grain 8 in Figure 4(c)).

Summarizing all the experimental results presented in this section, the main conclusion is that the resistance of the material to HIC damage may be improved significantly by reducing the relative proportion of $\{001\}$ //ND oriented grains and by increasing the proportion of grains with orientation of the $\{111\}$ //ND, $\{112\}$ //ND, and $\{011\}$ //ND fibers. Low-carbon steels having such a

crystallographic texture will show a significant reduction in the number of the weak, cleavagelike paths for crack propagation in the rolling plane.

E. Plastic Strain Induced by HIC

The EBSD technique also permits researchers to investigate the distribution of residual strain in the material.^[7] This advantage was used to study the distribution of plastic strain around HIC cracks. In order to do this qualitatively, the EBSD pattern quality parameter (IQ) was mapped for several HIC regions. It is well known that the IQ values decrease with increasing plastic deformation, which allows the distribution of plastic strain around cracks and crack tips to be mapped.^[7,18,19]

Figure 7 shows the SEM micrograph, the orientation map, and the EBSD pattern quality map of a HIC region containing two close interacting cracks in steel A. This interaction pattern was repeatedly observed in the investigated steels. The close cracks overlap and direct toward each other but never contact the opposite crack. In many observed cases, the deflection occurs through transgranular cleavagelike cracking along $\{001\}$ planes (grains A and B), and the region between the interacting crack tips shows a large residual plastic strain (Figure 7(c)).

In the interaction zone, the deformation occurs mostly heterogeneously by single or multiple slip induced by the opening and shear mixed-mode stress condition, which develops between the cracks as they approach each other and overlap.^[15,16] Hereafter, these two situations are called “before overlapping” (BO) and “after overlapping” (AO) interaction stages, respectively. It has been emphasized earlier that these stressing conditions are also responsible for the deflection of close spaced cracks (Figures 1(a), 4(a), and 7(a)) as well as for the triggering of crack nucleation between crack tips (Figure 4(a)).^[15,16,17]

Figure 7(c) provides evidence that the IQ map is a valuable tool to assess qualitatively the distribution of plastic strain associated with HIC.^[7,18] However, the influence of microtexture on the plastic strain induced by HIC can be better evaluated through the quantitative

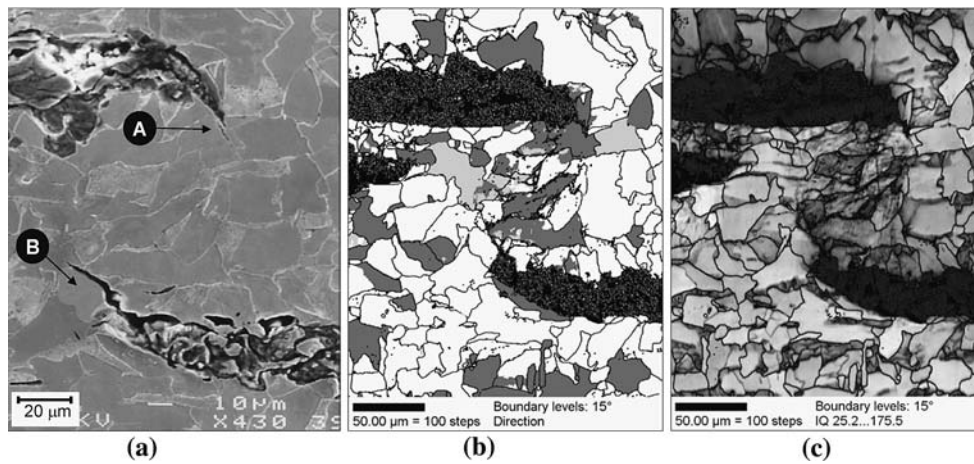


Fig. 7—Interaction between two close cracks in steel A. (a) SEM micrograph. (b) Orientation map (same color coding as in Fig. 3). (c) EBSD pattern quality (IQ) map; strain increasing with the darkness of the gray scale.

assessment of the in-grain orientation heterogeneities evidenced in Figure 7(c). This assessment can be carried out by mapping and analyzing the orientation spread of the grains in the HIC microstructure.

Figure 8(a) shows the grain orientation spread map for the HIC region shown in Figure 7. This map confirms that the grains between the overlapping cracks show the largest in-grain orientation scatter, which reaches 11 deg for grain 1 (identification key in Figure 8(c)). The large orientation scatter observed for the grains marked in Figure 8(c) is expected to be produced during the interaction process as the cracks approach and overlap. Therefore, the resulting in-grain orientation scattering should be related to the stress condition in both stages (AO and BO). The stress field associated with the BO condition has already been presented in Figure 5. For the sake of completeness, Figure 8(b) shows the maximum shear stress distribution for the AO condition in the same region. This distribution was computed following the methodology explained earlier (Figure 5(a)). However, to produce

Figure 8(b), the parameter d/a was chosen as -0.4 . It is worth noting that the sign of the maximum shear stress τ_{max} remains the same in Figures 5(c) and 8(b), while the plane on which this stress acts changes its orientation during the crack interaction process. Figures 5(c), 8(b), and 9 can be used to find the relationship between the state of stress before and after crack overlapping and the large plastic deformation suffered by the grains in the region between the interacting crack tips.

Let us analyze how plastic deformation has occurred in grain 1 (Figure 8(c)) whose orientation is close to $\{111\} \langle 121 \rangle$. The results presented in Figure 9(a) indicate that a very large cumulative (point-to-origin) misorientation develops along this grain as a result of its deformation by slip under the influence of grain-to-grain interaction. Yet, the nearest neighbor (point-to-point) misorientation profile crosses LABs not greater than 5 deg. This behavior was observed for all the grains marked in Figure 8(c).

Figure 9(b) shows the inverse pole figure of the maximum shear axis in the crystal reference system

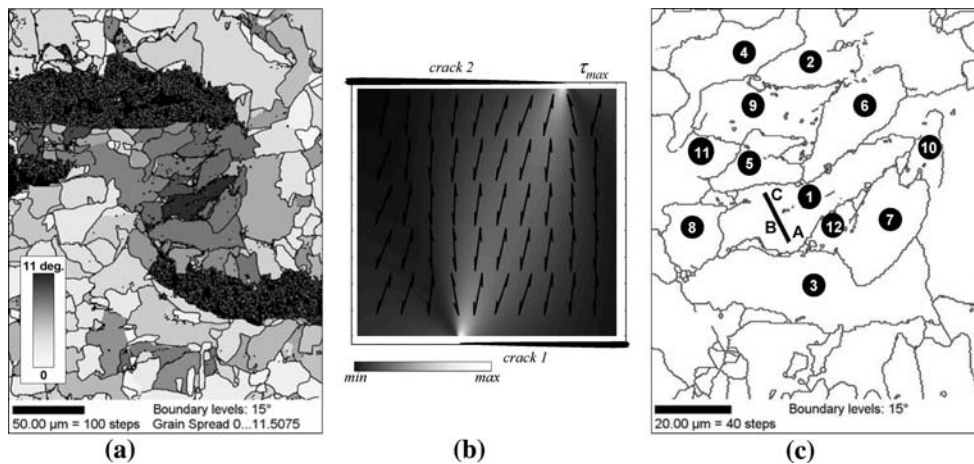


Fig. 8—(a) Grain average misorientation spread map of the HIC region as shown in Fig. 7 (a). (b) Maximum shear stress distribution in the region between the crack tips, computed as in Fig. 5 (a) with $d/a = -0.4$. (c) Grain identification key.

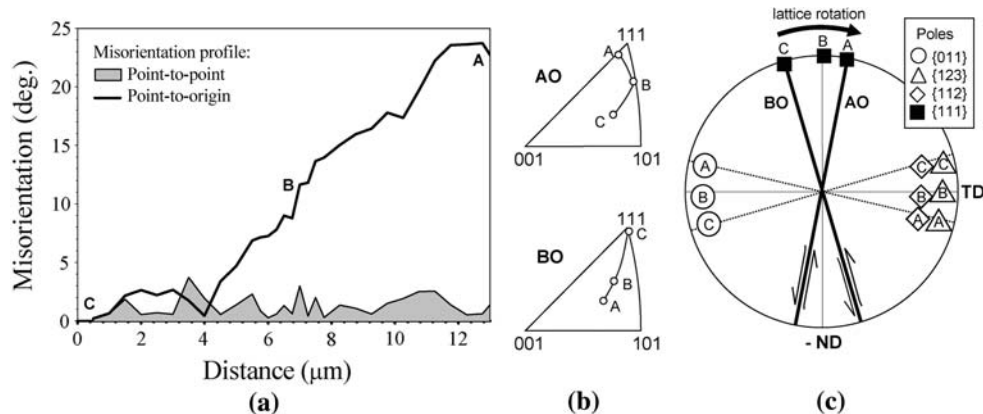


Fig. 9—Lattice reorientation by plastic deformation due crack interaction. (a) Misorientation profile along line A-C in grain 1 (Fig. 8 (c)). (b) Inverse pole figure of the maximum shear direction before crack-tip overlapping (BO) and after overlapping (AO). (c) Poles of the possible active slip systems at points A through C.

associated with grain 1. In this figure, BO and AO refer to the axes for the stress conditions before and after crack overlapping, respectively. The large cumulative misorientation observed in this grain (Figure 9(b)) is related to the rotation of the crystal $\langle 111 \rangle$ slip direction toward BO at point C and toward AO at point A. To further confirm this, Figure 9(c) shows that the reorientation of the lattice within this grain is such as to align the $\{110\}$, $\{112\}$, and $\{123\}$ slip planes to the maximum shear plane in each interaction stage. The orientation of the maximum shear planes, whose traces are also represented in Figure 9(c), can be easily obtained from the results presented in Figures 5(c) and 8(b) for the location occupied by the analyzed grain.

The main conclusion from the preceding analysis is that the plastic deformation of grain 1 started when the cracks were close enough to induce a shear stress greater than the critical shear stress and that this deformation continued during and after crack overlapping. The sense of the associated lattice rotation, indicated in the upper part of Figure 9(c) by a thick arrow, can be predicted from the rotation observed for the maximum shear plane from the BO (Figure 5(c)) to the AO stress condition (Figure 8(b)). Following this reasoning, it was also concluded that the lattice reorientation observed in grains 6–9 and 12 is due most probably to the fact that these grains deformed plastically just before crack overlapping. In contrast, grains 2–5, 10, and 11 deformed during and after crack overlapping as grain 1 did.

It is important to underline that the enhanced slip activity observed in the region between the interacting cracks decreases the driving force for their propagation and could thereby retard their growth. Besides, it reduces the probability of crack coalescence due to the shear stress relaxation by plastic deformation.^[15] Figures 5(c), 8(b), and 9 reveal the even more important fact that grains with orientations along the $\{111\}$ //ND fiber, e.g., grains 1–3 and 11, show more suitably oriented slip systems for large plastic deformation by extensive slip during both crack interaction stages (BO and AO).

These results clearly indicate that the presence of a strong $\{111\}$ //ND texture in the material could improve

its resistance to stepwise HIC by reducing the driving force for the growth of interacting cracks, with the consequent reduction in the probability of coalescence of closely spaced, non-coplanar cracks.

F. Role of Mesotexture on Crack Propagation

The influence of grain boundary texture, i.e., of mesotexture, on HIC was investigated by determining the statistics of grain boundaries across the crack paths and in noncracked regions. The results of this analysis are presented in Figure 10(a), which shows the proportion of low-angle, high-angle, and coincidence grain boundaries across HIC cracks and in those regions where HIC did not develop. A total of 861 boundaries were identified across the HIC cracks, while more than 10^5 boundaries were identified in the noncracked material.

The mesotexture along HIC paths shows a higher proportion of HABs and LABs than that observed in the noncracked regions. It also shows the lowest proportion of special CSL boundaries. The inset in Figure 10(a) shows that this proportion is even lower than that observed in a randomly oriented polycrystal. This indicates that intergranular HIC propagation occurs mainly along high-energy HABs, while CSLs and LABs provide a reduced number of propagation paths. Note that the $\Sigma 3''$ boundaries in low carbon steels should be classified as HABs, because, most probably, they are not generated by true single or multiple twinning.^[5] Examples of “texture induced” noncoherent twin boundaries are shown in Figure 10(b), in which some of the orientation relationships that classify as $\Sigma 3$ are marked in the $\varphi_2 = 45$ deg section of the Euler space.

The high proportion of LABs observed across crack paths was related to intergranular fracture along boundaries between grains with $\{001\}$ //ND orientation. This result (and that shown in Figure 6(a)) corroborates that the presence of a strong $\{001\}$ //ND fiber texture can increase the susceptibility of the material to HIC.

In contrast, the grain boundary statistics in the noncracked regions show the highest proportion of

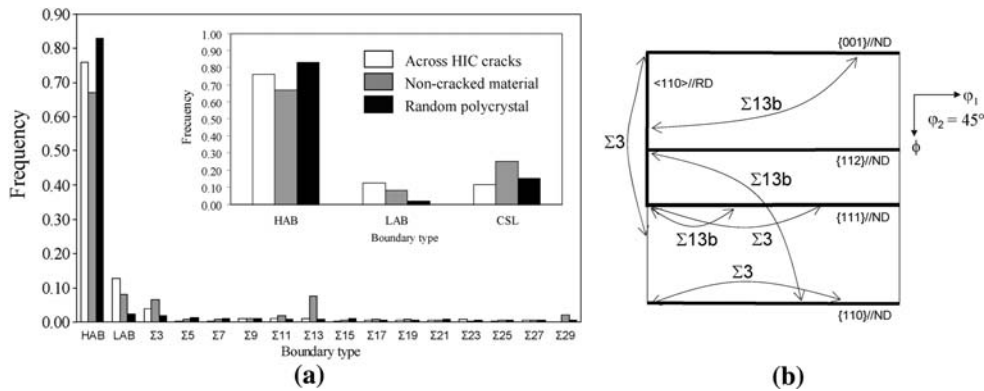


Fig. 10—(a) Grain boundary statistics along crack paths and in noncracked regions in steel A. (b) Examples of orientation relationships that classify as $\Sigma 3$ and $\Sigma 13b$ CSL grain boundaries in the $\phi_2 = 45$ deg section of the ODF.

CSL boundaries. This is especially noticeable for the $\Sigma 13b$, $\Sigma 11$ and $\Sigma 29a$ grain boundaries. The high proportion of $\Sigma 13b$ observed in these regions was found to be related to the presence of a relatively large proportion of grains with $\{111\}$ //ND orientation. Within this fiber, for example, the relationship between the $\{111\}\langle 110 \rangle$ and $\{111\}\langle 121 \rangle$ orientations is within 3 deg of the ideal orientation relationship that defines a $\Sigma 13b$ boundary (Figure 10(b)).

On the other hand, it has been reported^[20] that the energy of LABs with a misorientation axis close to $\langle 001 \rangle$ (e.g., those between $\{001\}$ //ND oriented neighbors) is higher than the energy of those with a rotation axis close to $\langle 111 \rangle$.

Therefore, with regard to mesotexture, a steel with a strong $\{111\}$ //ND fiber texture is expected to show a reduced susceptibility to HIC because of the increased presence of special CSLs and LABs with the lowest possible energy.

IV. CONCLUSIONS

In this work, the influence of crystallographic texture on HIC in low carbon steels for sour service piping has been investigated using X-ray and EBSD texture measurements. The following conclusions can be drawn.

1. It may be possible to improve the HIC resistance of low carbon steels to be used in wet hydrogen sulfide environments through crystallography texture control and grain boundary engineering.
2. Such an improvement could be achieved by using controlled rolling schedules. For example, warm rolling with finishing temperatures in the 600 °C to 800 °C range^[10,21] could be used to produce steel textures dominated by the $\{112\}$ //ND, $\{111\}$ //ND, and $\{011\}$ //ND texture fibers.
3. This texture is expected to reduce significantly the probability of HIC by reducing the $\{001\}$ //ND oriented regions and, consequently, the availability of weak transgranular and intergranular cleavage paths parallel to the rolling plane.
4. It may also decrease the probability of crack coalescence and stepwise HIC propagation through the

large local plastic deformation of the $\{111\}$ //ND oriented grains, which reduces the driving force for crack propagation and deflection in the pipe's radial direction.

5. Finally, it may increase the number of high resistance intergranular crack paths provided by coincidence site lattice and low-angle boundaries between grains of the $\{111\}$ //ND fiber.

ACKNOWLEDGMENTS

The authors thank D. Solas and E.S. Valladares for measuring the X-ray pole figures of the investigated steels and for processing the OIM data, respectively.

REFERENCES

1. M. Iboujdaini: *Uhlig's Corrosion Handbook*, 2nd ed., R. Winston Revie, ed., John Wiley & Sons Inc., New York, NY, 2000, pp. 205–20.
2. T. Hara, H. Asahi, and H. Ogawa: *Corrosion*, 2004, vol. 60 (12), pp. 1113–21.
3. E. Miyoshi, T. Tanaka, F. Terasaki, and A. Ikeda: *J. Eng. Ind.*, 1976, vol. 11, pp. 1221–30.
4. J.I. Verdeja, J. Asensio, and J.A. Pero-Sanz: *Mater. Charact.*, 2003, vol. 50, pp. 81–86.
5. T.G. Oakwood: *Metal Handbook*, 9th ed., vol. 13, *Corrosion*, ASM INTERNATIONAL, Materials Park, OH, 1987, pp. 531–46.
6. R.D. Kane and M.S. Cayard: *Review of Publisher Literature on Wet H₂S Cracking of Steels through 1989*, NACE International Publication 8X294, 2003 ed., NACE, Houston, TX, 2003.
7. V. Randle and O. Engler: *Introduction to Texture Analysis: Macrotexture, Microtexture and Orientation Mapping*, Francis & Taylor, London, 2003, pp. 3–58.
8. A.J. Wilkinson: *Phil. Mag. A*, 2001, vol. 81 (4), pp. 841–55.
9. U. Krupp, O. Duber, H.J. Christ, B. Kunkler, A. Schick, and C.P. Fritzen: *J. Microsc.*, 2003, vol. 213 (3), pp. 313–20.
10. R.K. Ray, J.J. Jonas, M.P. Butrón-Guillén, and J. Savoie: *ISIJ Int.*, 1994, vol. 34, pp. 927–42.
11. S.P. Lynch: in *Hydrogen Effects on Materials Behavior and Corrosion Deformation Interaction*, N.R. Moody, A.W. Thompson, R.E. Ricker, G.W. Was, and R.H. Jones, eds., TMS, Warrendale, PA, 2003, pp. 440–66.
12. *OIM Users Manual*, 2001 ed., TexSeM Laboratories Inc., Provo, UT, 2001, pp. 48–49.
13. *Evaluation of Pipeline and Pressure Vessel Steels for Resistance to Hydrogen-Induced Cracking*, NACE Standard Test Method TM0284-96, NACE, Houston, TX, 1997, pp. 1–10.

14. K. Pawlick: *Phys. Status Solidi*, 1986, vol. B134, pp. 477–83.
15. Y.Z. Wang, J.D. Atkinson, R. Akid, and R.N. Parkins: *Fatigue Fract. Eng. Mater. Struct.*, 1996, vol. 19, pp. 427–39.
16. D. Gross and T. Seelig: *Fracture Mechanics*, Springer-Verlag, Berlin, 2006, pp. 64–87.
17. Y.P. Li and C.H. Yang: *J. Mech. Mater. Struct.*, 2006, vol. 1 (1), pp. 147–62.
18. V. Venegas, F. Caleyo, J.L. González, T. Baudin, J.M. Hallen, and R. Penelle: *Scripta Mater.*, 2005, vol. 52, pp. 147–52.
19. M.A. Othon, L.N. Brewer, L.M. Young, and T.M. Angeliu: *Microsc. Microanal.*, 2002, vol. 8 (S02), pp. 698–99.
20. C.C. Yang, A.D. Rollet, and W.W. Mullins: *Scripta Mater.*, 2001, vol. 44, pp. 2735–74.
21. A. Haldar and R.K. Ray: *Mater. Sci. Eng. A*, 2005, vol. A391 (1–2), pp. 402–07.